



Fast and *in situ* releasing of active species confined in two-dimensional layers for superior overall electrochemical water splitting

Yayun Pu^{a,1}, Yufei Liu^{c,d,1}, Xiaosheng Tang^a, Qiang Huang^{a,*}, Limin Huang^{b,*}

^a School of Optoelectronic Engineering, Chongqing University of Posts and Telecommunications, No.2 Chongwen Road, Chongqing 400065, China

^b Department of Chemistry, Southern University of Science and Technology, No. 1088 Xueyuan Blvd, Shenzhen, Guangdong 518055, China

^c Key Laboratory of Optoelectronic Technology & Systems (Ministry of Education), College of Optoelectronic Engineering, Chongqing University, Chongqing 400044, China

^d Centre for Intelligent Sensing Technology, College of Optoelectronic Engineering, Chongqing University, Chongqing 400044, China

ARTICLE INFO

Keywords:

Overall water splitting
Layered metal oxide
Intercalation
Electrostatic interaction
In situ structure evolution

ABSTRACT

Realizing bifunctional catalysts for the HER and OER in a unified environment bears the promising goal of reducing the cost and complexity of electrolyzer devices. Dual atoms configuration intrinsically active to hydrogen/oxygen evolution is a feasible way to achieve that target. In this work, Co, Ir active species were selected to be inserted into the interlayer space of layered V_2O_5 , forming a two-dimensional confined structure that significantly improves the atomic efficiency. During the electrochemical water splitting in alkaline medium, the V-O framework that encapsulated the active species in layered V_2O_5 was collapsed and disrupted due to its acidic nature. The HER/OER active Co, Ir were readily released and exposed to the reactant. *In situ* structure evolution was monitored and elaborately analyzed by *operando* Raman, TEM and XPS characterizations. Further, DFT calculation disclosed that the Co atom was covalently stabilized by the nearest oxygen that leads to electron-depleted Co. The stabilization of Ir was achieved by forming both a covalent bond with oxygen and a metallic bond with sublayer V. This, however, resulted in a changed electron distribution in Ir, leading to better binding with oxygenate intermediates and improved OER activity. As for the alkaline HER, the potential determining step (PDS) of $IrCo@V_2O_5$ is predominately determined as the OH desorption, regardless of the H evolution pathway of Volmer-Tafel or Volmer-Heyrovsky. The bifunctional $IrCo@V_2O_5$ acted like a “Trojan Horse” and achieved an ultrahigh mass activity of 848 $A\ g_{Co, Ir}^{-1}$ for the OER and 461 $A\ g_{Co, Ir}^{-1}$ for the HER. This work provides new insight into creating highly effective electrocatalysts via the *in situ* releasing methodology.

1. Introduction

Electrochemical splitting of water has been considered as the most promising strategy to generate hydrogen fuel [1]. In an electrolyzer system, different catalysts are often used for hydrogen evolution reaction (HER) on the cathode and oxygen evolution reaction (OER) on the anode. For example, Pt/C and Ru/Ir oxides are current benchmark catalysts for HER and OER, respectively [2,3]. Exploring a single catalyst with bifunction towards HER/OER in the same catalytic environment is essentially important, since it can eliminate the complication of device and possible contaminations. The development of low-cost and high-efficient bifunctional catalysts undoubtedly bears both scientific and industrial significance. It is recognized that the HER and OER are

controlled by different mechanisms, which means that the catalysts required for each process are fundamentally different due to the optimal adsorption energy of the reactants. For the HER, optimal binding of H is generally the key to superior kinetics [4]. In contrast, the adsorption energy of $*OH$, $*O$ and $*OOH$ intermediates determines the efficiency of OER [5,6]. The inborn difference requires introducing both HER/OER active species into an integrated catalyst and optimizing their electronic structure concertedly.

In alkaline media, substantial progress has been made on Ni, Fe, Co-based materials towards bifunctional water splitting [7–10]. However, the Ni, Fe, Co oxide/hydroxides are considered inherently poor active for HER. Ir, Ru with fantastic H affinity often exhibit superior HER activity at alkaline conditions. It is reasonable to construct a diatom system

* Corresponding authors.

E-mail addresses: qhuang1986@163.com (Q. Huang), huanglm@sustech.edu.cn (L. Huang).

¹ These authors contributed equally.

based on Co and Ir. Considering the high cost and scarcity of noble metals, a new strategy to improve atomic efficiency is fundamentally required. In this context, to achieve functional single-atom or single-layer atoms, it is effective to contain the active species within two-dimensional tunneled materials [11–13]. Low loading of catalytically active sites can exhibit ultrahigh intrinsic activity. However, the confined configuration with a rigid framework can cause issues with mass transport, as reactants and products have to diffuse throughout the entire two-dimensional tunnel. Exposing atoms confined to the layer center is a new challenge to further enhance the atomic activity.

Herein, we newly report a fast *in situ* releasing strategy by selecting layered V_2O_5 as the ‘soft’ 3D framework to confine a small portion of active Co, Ir species. With the inborn acidic characters, layered V_2O_5 collapsed and partially dissolved in the alkaline electrocatalysis, behaving like the ‘Trojan Horse’. The active species was, therefore, *in situ* exposed and released to catalyze both OER and HER efficiently. As-prepared $IrCo@V_2O_5$ ($IrCo@VO$) exhibits excellent bifunction of HER ($\eta_{10} = 92$ mV) and OER ($\eta_{10} = 280$ mV) activity in alkaline media. For the overall water splitting measurement, applied potential at 1.607 V vs. RHE, the $IrCo@VO$ can achieve an overall current density of 10 mA cm^{-2} . The ultrahigh mass activity of $848 \text{ A g}_{Co, Ir}^{-1}$ for the OER and $461 \text{ A g}_{Co, Ir}^{-1}$ for the HER has been achieved. By taking advantage of two-dimensional confinement for highly dispersed active sites and delivering a quick release of active sites by *in situ* destroying the layered framework, this work provides a different insight into the high-efficient catalyst design.

2. Experimental section

2.1. Preparation of Co intercalated V_2O_5 ($Co@VO$)

The $Co@VO$ was synthesized by microwave hydrothermal method. Typically, 1 mmol of V_2O_5 (99.0 %, Macklin) was homogeneously dispersed in 20 mL ultrapure water in a glass tube by 20 min ultrasonication. 2 mL H_2O_2 (30 %, Sinopharm) was added under magnetic stirring until clear orange solution obtained. Then, 0.1 mmol Co ($(NO_3)_2 \cdot 6H_2O$ (99 %, Aladdin) was added into the above solution with stirring of 30 min. The prepared solution was sealed, placed into a microwave reactor (CEM, Discover SP), heated to 120°C (power 200 W) and held for 1 h. Brick red precipitates were collected through centrifugation and then washed with ultrapure water three times. The resultant solid was dried by lyophilization at -78°C . H_2O intercalated V_2O_5 (HVO) was prepared with the same procedure except adding Co sources.

2.1.1. Preparation of $IrCo@VO$

90 mg as-synthesized $Co@VO$ was dispersed in 30 mL ultrapure water and sonicated for 20 min to get a homogeneously dispersed suspension. Separately, 1 mL H_2IrCl_6 solution (1 mg mL^{-1}) was mixed with a series concentration of NH_4OH solution (30 %) with Ir: $NH_3 = 1:1, 1:4, 1:6, 1:10, 1:50$ and $1:100$. The Ir- NH solutions were added to $Co@VO$ suspension dropwise under 800 rpm magnetic stirring. After stirring overnight, $IrCo@VO$ powder was obtained by lyophilization at -78°C .

2.2. Materials characterizations

The particle morphology was characterized using a scanning electron microscopy (SEM, Zeiss with Oxford Instruments EDS attachment) with an acceleration voltage of 15 kV and probing current of 1 nA. Transmission electron microscopy (TEM) was performed on a FEI Tecnai G2 F30 with an acceleration voltage of 300 kV. High-angle annular dark field scanning transmission electron microscopy (HAADF-STEM) imaging experiments were carried out on a FEI Talos F200X microscope operated at 200 kV. Powder X-ray diffraction (PXRD) was performed on a Rigaku Smartlab-9Kw X-ray diffractometer with Cu $K\alpha$ radiation ($\lambda = 1.5406 \text{ \AA}$) at room temperature. XRD data were recorded between 5° – 65° with a step size of 0.02° . Inductively Coupled Plasma Mass Spectrometry (ICP-MS) measurement was carried out in an Agilent 7700x

equipment. The XPS analyses were performed on a PHI 5000 VersaProbe III spectrometer using a monochromatic Al K(α) X-ray source, with most used X-ray settings being 200 μm , 50 W, 15 kV. The PHI 5000 VersaProbe III charge neutralization system was used on all specimens. Charge neutralization was deemed to have been fully achieved by monitoring the C 1 s peak positions, which remained unchanged throughout the experiment.

2.3. Electrochemical characterization

All the electrochemical measurements were performed in a standard three-electrode setup. Electrochemical measurements were performed using an electrochemical workstation CHI 760e. A high surface area Pt foil (OER) and carbon rod (HER) were used as the counter electrode (CE), and Hg/HgO (1 M KOH) connected via a luggin capillary was used as the reference electrode (RE). Alkaline electrolyte was freshly prepared by dissolution of KOH flakes (Aladdin, semiconductor grade, 99.99 %) in ultrapure water. The electrolytes were purged with Ar (99.99) for at least 30 min prior to measurements and Ar stream flow above the solution during measurements. Glassy carbon (GC) diameter of 5 mm and carbon paper with a geometric area of 0.2 cm^2 were used as a support for the nanoparticles. After the deposition of catalyst, 10 μL prepared diluted Nafion solution was dropped on the surface of electrode and dried in oven. The final loading of each electrode was $\sim 0.2 \text{ mg}_{\text{catalyst}} \text{ cm}^{-2}$. Cyclic voltammetries (CVs) were performed firstly until the curves became stable. After then, linear scanning voltammetries (LSVs) were recorded in a potential window of 0.8–1.76 V vs. RHE for OER with a scan rate of 5 mV s^{-1} . For the HER, the potential was scanned from 0.1 to -0.5 V vs. RHE. All the measurements were recorded at 1600 rpm in order to avoid the interference of O_2 bubbles during the OER. The Ohmic resistances of the electrochemical system were obtained from CHI 760e used for iR-correction. Amperometric i-t measurement was kept at 1.51 V vs. RHE for OER and -0.09 V vs. RHE for HER during 24 h.

2.4. Operando Raman spectroscopy test

Raman scattering spectra were collected using a confocal Lase Raman Spectrome (HORIBA LabRAM) with a 532 nm He-Ne laser (0.2 mW). Acquisition parameters are 10 s exposure time and 5 cycles. The homemade Raman electrolysis cell consisted of three electrodes including a counter electrode (Pt wire), a reference electrode (Ag/AgCl), and carbon paper with catalysts as the working electrode. Raman data were collected after a 300 s holding at each applied potential.

2.5. Density functional theory methods

In this work, all the calculations were performed by using the Perdew-Burke-Ernzerhof (PBE) generalized gradient approximation (GGA) functional [14]. Spin-polarized DFT+U was applied for the Co and V to correct the DFT self-interaction errors, the U for Co is set as 3.5 eV and 3.4 eV for V [15,16]. The plane wave cutoff energy was set at 500 eV and the Brillouin zone was using $3 \times 3 \times 1$ Monkhorst-Pack grid. The maximum force limit, maximum energy variation tolerance and maximum displacement were set as 0.02 eV \AA^{-1} , $10^{-5} \text{ eV per atom}$ and 0.001 \AA . The self-consistent field (SCF) tolerance was set as $2 \times 10^{-6} \text{ eV per atom}$. A vacuum distance of 20 \AA was set in Z axis to avoid the periodic interaction. Free Energy under standard conditions (298 K) for the OER/HER process was calculated. Gibbs free Energy (ΔG) is computed by the equation of $\Delta G = \Delta E + \Delta E_{ZPE} - T\Delta S$, where the ΔE is the different energy between each reaction step, ΔE_{ZPE} is the difference between zero-point energy of each reaction step, ΔS is the difference between vibrational entropy of each reaction step [17].

3. Results and discussion

3.1. Electrocatalyst preparation and characterization

The Co inserted δ -V₂O₅ was synthesized by facial microwave-assisted strategy, followed by intercalation of Ir species via electrostatic interaction to achieve a Ir_{0.086}Co_{0.12}@V₂O₅ (IrCo@VO) synthesis at room temperature (details in experimental section). Since a net negative charge was found on Co²⁺ intercalated V₂O₅ (Co@VO), any cations or complex with positive charge can be employed to interact with Co@VO in aqueous solution (Fig. S1). The positive Ir complex was prepared by mixing Chloroiridic acid with optimal concentration ammonium. UV-Vis spectra in Fig. S2 show the [IrCl₆]²⁻ character gradually disappeared with the increase of ammonium concentration, demonstrating the successful replacement of coordinated ligands around Ir atoms. Positive Ir complex was inserted into the Co@VO interlayer via electrostatic interaction, resulting in flocculation of well-dispersed Co@VO nano-sheet suspension.

The morphology was firstly characterized by scanning electron microscopy (SEM) and transmission electron microscopy (TEM). As shown in Fig. 1a-d, flower-like hierarchical structure IrCo@VO is constructed by thin nanosheets interconnected with each other, showing a smooth surface. The decoration of Ir does not change the morphology of pristine Co@VO, and both of them keep identical morphology and size (Fig. S3, S4). A lattice fringe of 11.2 Å at the wrinkle region in Fig. 1c can be correlated to (001) crystal face, the interlayer gallery where Co²⁺ cations are accommodated. High-angle annular dark-field transmission

electron microscopy (HAADF-STEM) and the corresponding energy-dispersive X-ray spectrum (EDS) elemental mapping images clearly show the uniformly dispersed elements of V, O, Co, Ir over the hierarchical structure. The relatively weaker intensity of Co and Ir indicates a small amount of incorporation. Inductively coupled plasma mass spectroscopy (ICP-MS) reveals the mole ratio of each meal element (Table S1), with Ir: Co: V = 1: 1.39: 23.27. Thus, the formula of IrCo@VO can be determined as Ir_{0.086}Co_{0.12}@V₂O₅. The crystal structure of IrCo@VO is confirmed by X-ray diffraction (XRD) patterns, as shown in Fig. 1f. All the signals can be assigned to the typical δ -V₂O₅ structure with molecule intercalation [18]. The (001) plane in IrCo@VO shifted to a higher degree as compared to that in pristine Co@VO, with the interlayer distance shrinking from 13.86 Å to 11.3 Å. It is identical to the TEM result in Fig. 1c. The decrease of interlayer distance can be linked to the intercalation of Ir species into the gallery since the higher valence state of Ir caused a stronger interaction with the terminated O of V-O slab. This was supported by the comparison of Co intercalated δ -V₂O₅ and CuCo intercalated δ -V₂O₅ in Fig. S5. Cu²⁺ with the same valence state as Co²⁺ did not change the interlayer structure. Successful intercalation of Ir species was further confirmed by the Raman measurement, as shown in Fig. S6. All the Raman signals were kept the same for IrCo@VO and Co@VO except the one at ca. 880 cm⁻¹. This blue-shifted peak is associated with the interlayer vibration mode of layered metal oxide [19]. Our control Raman experiments of changing the interlayer species of Co and H₂O well confirmed it (Fig. S7).

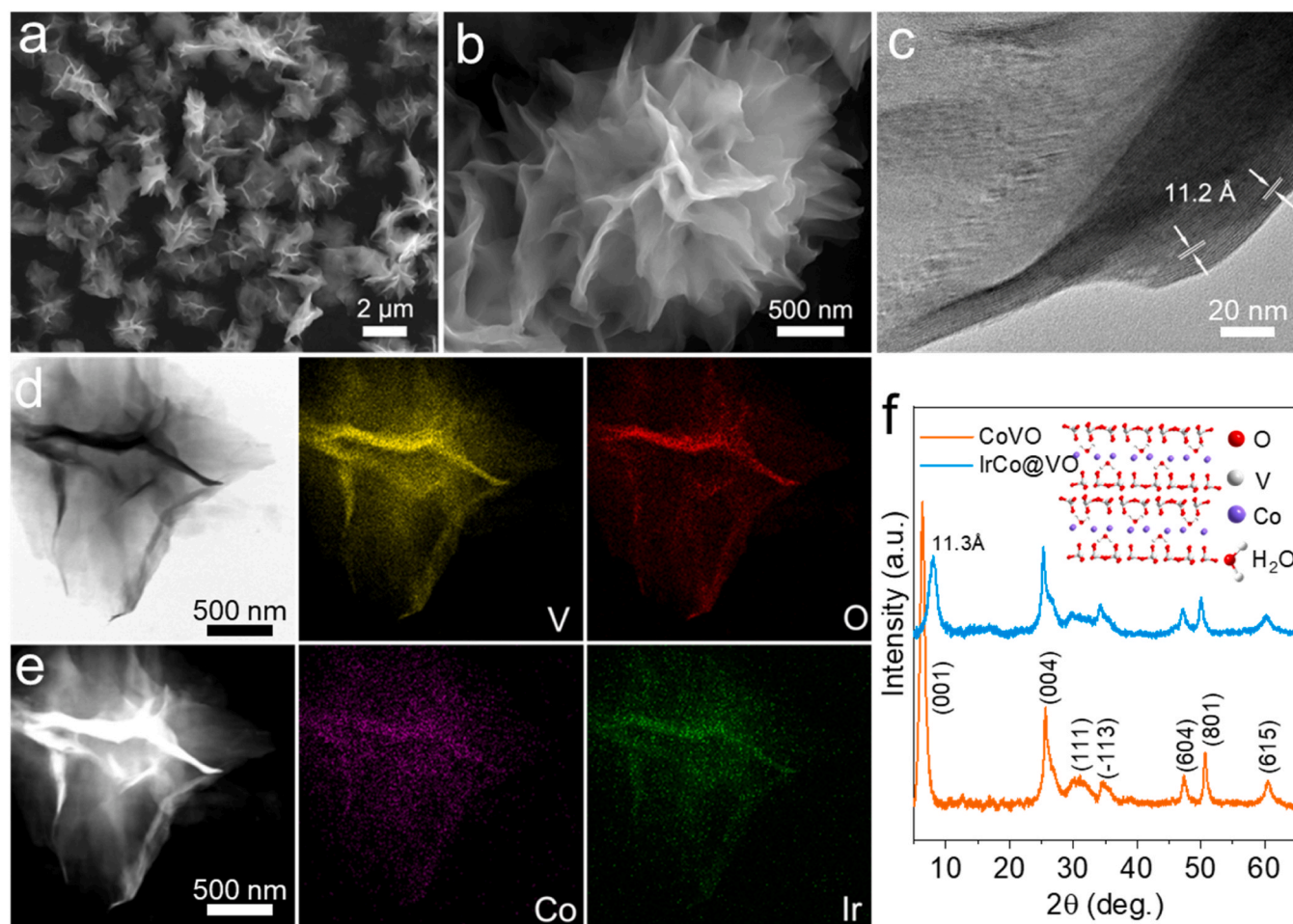


Fig. 1. (a), (b) SEM images, (c) TEM images and (d), (e) HAADF-STEM images with EDS mappings of IrCo@VO, (f) X-ray diffraction patterns of Co@VO and IrCo@VO, with Co@VO crystal structure plot inset.

3.2. Study of electrochemical performance

The catalytic OER performance of IrCo@VO with control samples was evaluated in 1 M KOH electrolyte. Geometrical current densities normalized by the glassy carbon electrode (GCE) surface area are presented in Fig. 2a. The IrCo@VO only requires an overpotential of 281 mV to reach a current density of 10 mA cm^{-2} (η_{10}), which outperforms the benchmark commercial IrO_2 nanoparticles of 350 mV. In addition, to investigate the active sites for electrocatalytic water splitting, the H_2O intercalated V_2O_5 (HVO), Co decorated on HVO (Co@HVO), Co intercalated V_2O_5 (Co@VO) were selected for comparison. The poor activity of HVO for OER implies the sluggish kinetics of vanadium sites, where V is not facilitated to the OH adsorption. Since HVO shows negative net charge, a trace amount of Co^{2+} can be introduced on the surface via electrostatic interaction (details in the experimental section). In contrast to the HVO, Co@HVO shows a significantly improved OER activity, which is comparable to the Co@VO sample. As present in Fig. 2c, the η_{10} for Co@HVO and Co@VO are 380 and

385 mV, respectively. This clearly demonstrates the contribution of Co species for OER catalysis, despite the location of Co site either on the surface or intercalated in the gallery. On the base of Co@VO, Ir species were incorporated to further enhance the OER catalytic performance. Remarkably, the OER onset potential of IrCo@VO shifted from 1.56 V to 1.41 V vs. RHE. Introducing Ir into Co@VO significantly reduces the energy barrier of four consecutive steps of the OER process. The measured Tafel slope of all samples are close to each other, with 62 mV dec^{-1} for IrCo@VO, 63 mV dec^{-1} for IrO_2 , 65 mV dec^{-1} for Co@VO, and 60 mV dec^{-1} for Co@HVO.

The polarization curves of samples towards hydrogen evolution activity in 1 M KOH are presented in Fig. 2d. Similar to the OER activity, IrCo@VO shows excellent HER activity close to the commercial Pt/C. The overpotential of IrCo@VO at $j = 10 \text{ mA cm}^{-2}$ is 90 mV, which is slightly larger than 85 mV of Pt/C. Besides the overpotential, their Tafel slopes are also close, with 64 mV dec^{-1} for IrCo@VO and 67 mV dec^{-1} for Pt/C. In terms of the bare Co@VO sample, without Ir doping the η_{10} is distinctly increased to 258 mV, implying that the Ir species has

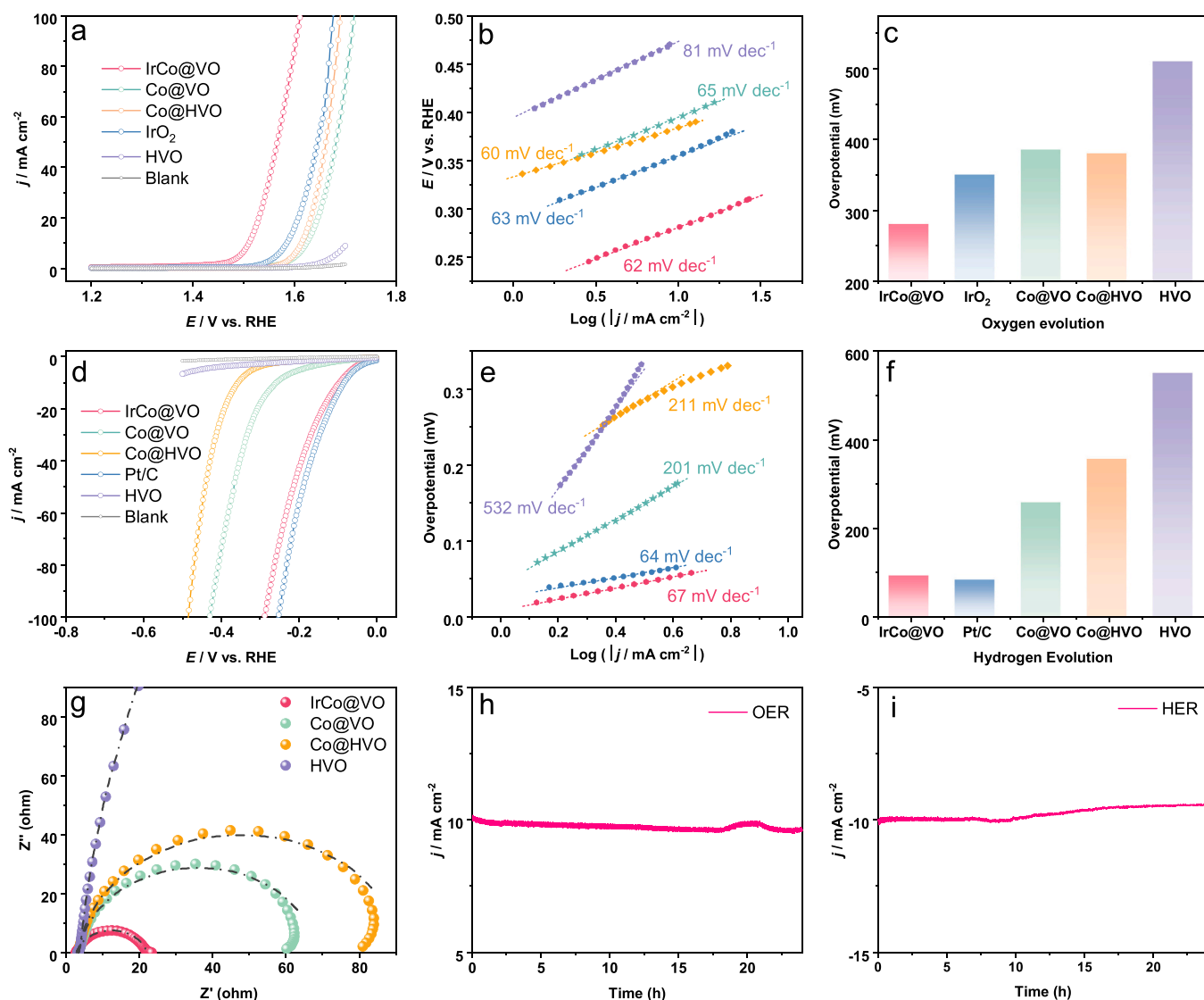


Fig. 2. Electrocatalytic OER measurements of (a) LSV curves of different catalysts measured at 1 M KOH electrolyte, with a scan rate of 5 mV s^{-1} . (b) corresponding Tafel slopes (c) comparison of overpotential to reach current density of 10 mA cm^{-2} on tested catalysts. Electrocatalytic HER measurements of (d) LSV curves of different catalysts measured at 1 M KOH electrolyte, with a scan rate of 5 mV s^{-1} . (e) corresponding Tafel slopes (f) comparison of overpotential to reach current density of 10 mA cm^{-2} on tested catalysts. (g) EIS of catalysts at η of 90 mV in HER test (dot-dash line denotes fit curves), (h) chronoamperometry test of IrCo@VO (h) at 1.51 V vs. RHE for OER (i) at -0.96 V vs. RHE for HER.

significantly improved HER activity. The Tafel slope of Co@VO increases to 201 mV dec^{-1} , indicating the difficulty of dissociating H_2O molecules and binding H on the active site. Like the OER counterpart, HVO requires a fairly high overpotential to drive the catalytic process, suggesting a poor interaction of H_2O molecules on V sites. The charge transfer resistance (R_{ct}) commonly reflects the kinetics of the catalytic reaction that occurs at the catalyst-electrolyte interface. Electrochemical impedance spectrometry (EIS) was performed. As depicted in Fig. 2g, on the basis of fitted data the R_{ct} for IrCo@VO is only 19.25Ω , which is much smaller than 62.64Ω for Co@VO, 86.90Ω for Co@HVO and 984.60Ω for HVO. The smallest semicircle radius suggests the fastest electron transfer between active sites and adsorption species. Identical variation trends of the EIS measured in OER condition were displayed in Fig. S9. In addition, time-dependent OER/HER current density tests were conducted to evaluate the stability of IrCo@VO under long-term catalytic operation. OER i-t curves in Fig. 2h reveal that a near 96 % retention rate was obtained over 24 h, the value for HER in Fig. 2i is 94.8 %. These long-term stability tests show that the IrCo@VO can deliver an excellent stable activity. The prepared catalyst was applied in a two electrodes system to examine the overall water-splitting performance.

As can be seen in Fig. S10, IrCo@VO catalyst shows better performance than the PtC/IrO₂ pair, requiring 70 mV lower overpotential to drive the 10 mA cm^{-2} current density than PtC/IrO₂.

3.3. Structure evolution evaluation

Since the layered V_2O_5 is an acidic type metal oxide, the structure evolution in alkaline medium should be considered and evaluated. Firstly, *operando* Raman was performed to identify the phase evolution during the electrolysis. In Fig. 3a, the anode OER showed that the initial layered Co intercalated V_2O_5 vibrational signals disappeared as the potential applied at 1.2 V vs. RHE in 1 M KOH. Only a single peak associated with the V-O stretching at 687 cm^{-1} remained [18]. Details of vibrations of IrCo@VO are presented in Fig. S5. At the same time, a broad hump in the range of 380–650 starts to emerge. Deconvolution of this broad peak is presented in Fig. 3b. Peaks at 459 and 580 cm^{-1} can be associated with the vibration modes of Co-O vibrations [20]. The signal at 495 cm^{-1} originates from the Ir-O vibration of amorphous IrO_x [21]. As the potential increased to the oxygen evolution region, Raman spectra kept the same, indicating that the active species are Co-Ir couple

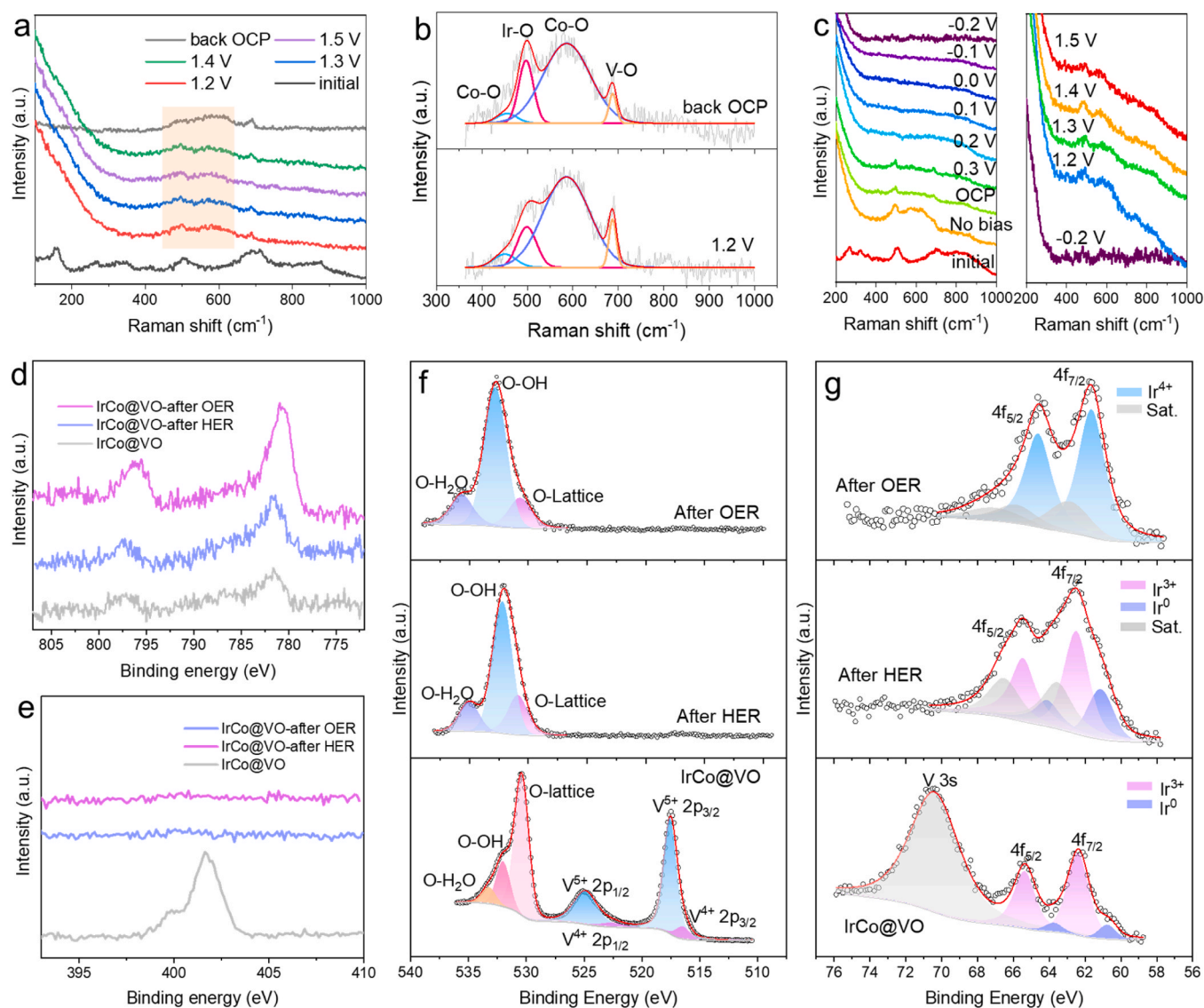


Fig. 3. *Operando* Raman spectra in 1 M KOH solution of (a) OER, (b) fitting results of Raman spectra at 1.2 V and back OCP. (c) HER, the potential window of the right panel reverses back to the oxidation region after the HER in the left panel. (d) high resolution Co 2p spectra of IrCo@VO before and after electrolysis, (e) Cl 2p, (f) O1s and V 2p spectra of IrCo@VO before and after electrolysis.

oxyhydroxide. Upon comparing the fitted peaks change at 1.2 V and at back OCP, the ratio of Ir-O/V-O decreases from 4.14 to 2.20, indicating the Ir-O species should be the active sites for OER. This was confirmed by our DFT calculation in Fig. 6 and Fig. S17, the adsorption energy of OH on Ir site is 0.02 eV, better optimized than the case of Co site (−0.21 eV) that facilitates the subsequent *O formation.

In the case of HER, after the catalyst was immersed into the electrolyte, the surface structure of layered V_2O_5 evolved into the Co-Ir bonded hydroxide. As the potential changed from 0.3 V vs. RHE to −0.2 V vs. RHE, the Co-O signal disappeared first and the Ir-O signal kept until the potential reached 0 V. Our DFT calculation in Fig. 7 shows that the H on the Co site while the OH group on the Ir site required

smaller energy to drive the H_2O reduction. The Ir shows more optimized oxygen affinity than Co, which matches with the *operando* Raman measurement well.

The structure evolution is well detected by the XPS. Fig. 3d shows that Co 2p spectra of IrCo@VO after HER kept the same valence as the pristine catalyst. Combined with the *operando* Raman measurement, it implies that the surface Co was supposed to be fully exposed during the HER process and not be reduced to metallic Co species. Under the OER condition, Co was oxidized to a higher state after the anodic catalysis, as the distance between 2p3 and 2p1 shrinks to 15.5 compared to the pristine one. It is suggested that the separation between two peaks can be associated with the oxidation state of Co, that 16.0 eV for Co^{3+} and

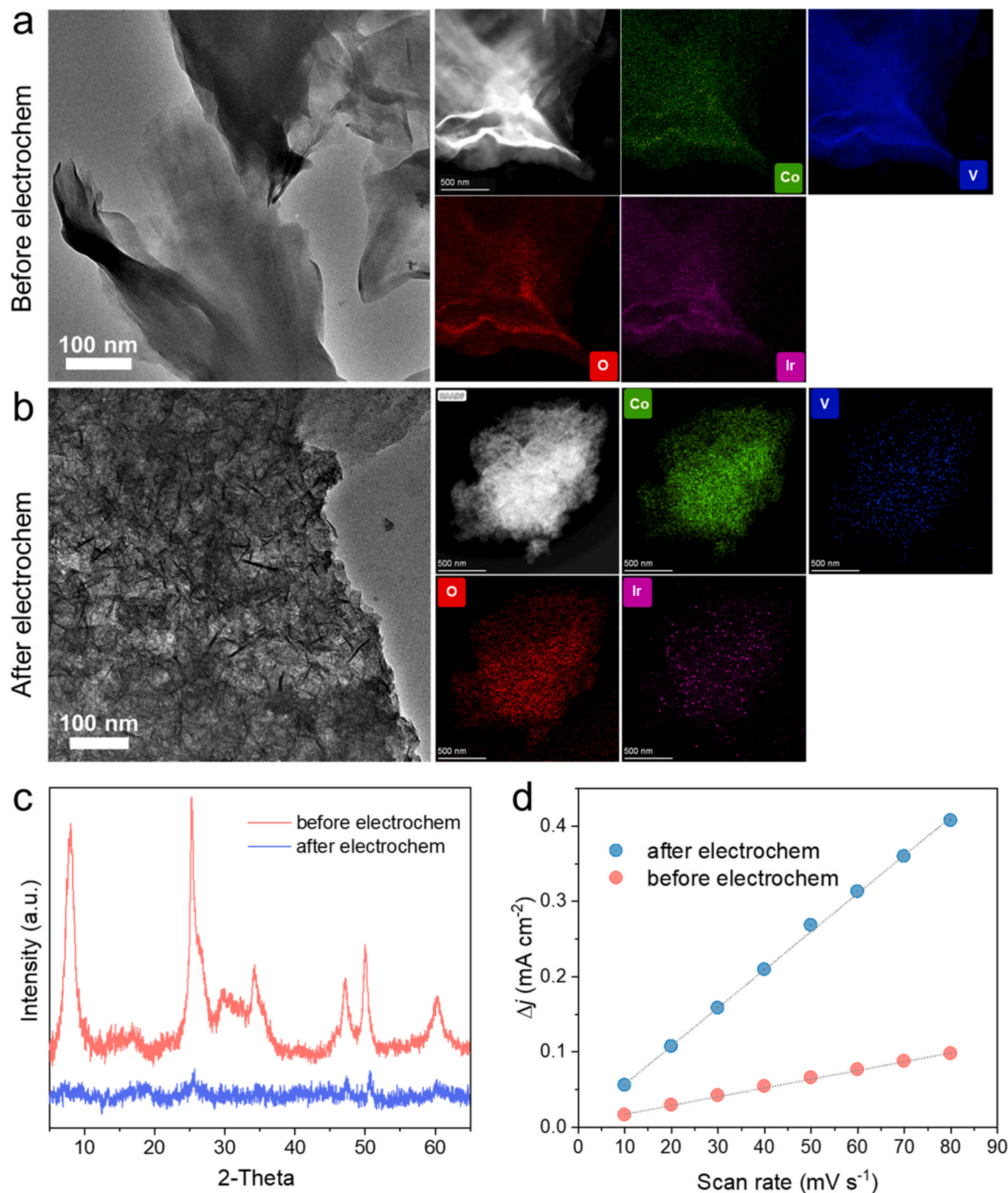


Fig. 4. TEM-EDS of (a) before (b) after the electrochemical reaction. (c) the XRD patterns (d) electrochemical active area calculations of IrCo@VO before/after electrochemical reaction.

15.0 eV for Co^{2+} [22,23]. The N-containing ligand was first found on as-synthesized IrCo@VO (Fig. 3e), which should be bonded with Ir to intercalate into the V_2O_5 interlayer. During electrocatalysis, N was detached from the catalyst, which aligns with previous literature where the Cl ligand in IrCl_6 group intercalated in NiFe LDH was released in electroreduction [24]. In addition, XPS data confirmed that surface V_2O_5 collapsed, evidenced by the disappeared V 2p and 3 s signals next to the binding energy of O1s and Ir 4 f (Fig. 3f,g). In detail, the active site is favorable to bind with the OH group from electrolyte or the dissociation of H_2O , as confirmed by the sharply increased O-OH brand after electrolysis in Fig. 3f. The fitting of Ir 4 f spectra was referenced to the literature [25]. Ir^{3+} was the majority state in the as-synthesized IrCo@VO , which overlapped with the V 3 s spectra. After the HER, the amount of Ir^0 increased, indicating the partial reduction of Ir species accompanied by the departure of coordinated N-containing ligands. Different from the HER, the Ir was oxidized to Ir^{4+} during OER, making it the dominant state.

Except for the *operando* Raman and XPS analysis, TEM coupled EDS was performed to study the structure evolution of the ‘Trojan Horse’ catalyst. As shown in Fig. 4a,b and Fig. S11 the surface morphology of IrCo@VO changed significantly after electrolysis in alkaline medium. Compared to the original smooth and clean surface of nanoflakes, new ultrafine nanosheets formed randomly on the outmost surface. EDS analysis shows that the signal intensity of V reduced significantly, which is consistent with the XPS results. XRD in Fig. 4c and Fig. S12 confirmed the collapsing of long-range ordered structure of the layered V_2O_5 , with significantly reduced diffraction peaks. Electrochemical surface area (ECSA) was calculated by plotting the current density difference vs. scan rates (Fig. S13). Fig. 4d shows that the ECSA after OER electrocatalysis increased by 5-fold compared to its initial state, which is consistent with the morphology change in Fig. 4b. Similar but not totally identical results were obtained in the case of HER, as shown in Fig. S11 and S15, since the catalyst was subjected to different potentials of reduction and oxidation.

3.4. Mechanism study

To gain a deeper insight into the bifunctionality of the catalyst for OER/HER, DFT calculations were performed. The electron density difference (EDD) of IrCo@VO is presented in Fig. 5a. For the Co site on the left, electrons mainly accumulated at the Co–O bond, implying a firm stabilization of Co by the surface O. For the Ir site on the right, a fairly different environment was formed. The Ir atom was stabilized by Ir–O covalent bonds and an Ir–Ti metallic bond. The electron density flow in

the Ir–O bond is clearly weaker than that in the Ir–V bond. This confirms that OH/ H_2O gained an optimized binding to Ir in the electrolyte, as supported by the Raman and XPS results. Upon the population analysis in Fig. 5b,c Co loses more electrons to form a well bond with oxygen compared to the adjacent Ir. The Ti atom bonded with Ir gained a small portion of electrons from Ir, which agrees with the EDD results.

The Gibbs free energy of $^*\text{O}$, $^*\text{OH}$ and $^*\text{OOH}$ of IrCo@VO have been calculated and plotted in Fig. 6. The Ir@CoOOH was constructed for comparison (Fig. S16). Firstly, the active site of both Co and Ir were examined within the IrCo@VO that confirmed the Ir site is more favorable in catalyzing the OER (Fig. S18). The comparison of IrCo@VO and Ir@CoOOH shows that the Ir on the CoOOH surface shows greater affinity towards the oxygen. The reactant OH can be easily chemically adsorbed on the Ir site in an exothermic step. However, the strong adsorption causes a comparable stable $^*\text{O}$ intermediate, which has to overcome a larger energy barrier to realize the $^*\text{OOH}$ formation. This flaw was improved in the case of IrCo@VO , where the binding energy of the oxygen-containing group was optimized. It could be linked to the redistribution of electron density that the V–Ir bond formation leads to less charge transfer from Ir to oxygen, as confirmed by the results in Fig. 5. The electron deficiency of Ir was alleviated, which resulted in a weaker OH binding strength on Ir. Therefore, the $^*\text{OOH}$ formation on IrCo@VO becomes easier, and the potential determining step (PDS) requires less energy of 2.1 eV.

In the case of catalyzing HER in alkaline medium, the dissociation of H_2O molecules should be considered. The reactive site of Ir and Co for H and OH adsorption/desorption were evaluated in both the Volmer-Tafel (V-T) pathway and the Volmer-Heyrovsky (V-H) pathway. Fig. 7 shows that in both reaction pathways, H evolution on the Co site coupled with the OH adsorption/desorption on the Ir site is the optimal solution for H_2O reduction. Despite the different energy barriers for $^*\text{H} \rightarrow \text{H}_2$ in the Tafel and the Heyrovsky steps, it is not the limiting step in the global scope. In the case of $^*\text{H}$ on Ir and $^*\text{OH}$ on Co, the strong binding of OH on Co made the desorption difficult, gaining a PDS of 1.05 eV in both V-T and V-H reaction pathways. Our results have confirmed that the HER activity is primarily controlled by the OH leaving from the catalyst surface in alkaline medium, regardless of how the H is binding with the active site. Koper’s group reported that the $^*\text{OH}$ binding strength was directly correlated to the activation energy that plays an important role in alkaline HER [26]. Our work clarifies the importance of synergy between the dual active sites.

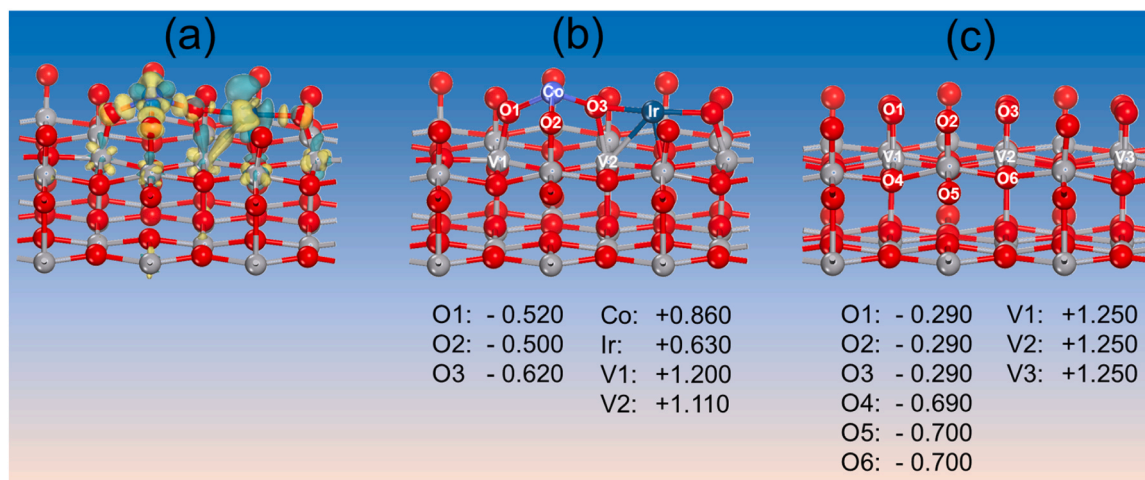


Fig. 5. Crystal structure of the (a) electron density difference of IrCo@VO , charge population of (b) IrCo@VO and (c) VO. The yellow region denotes electron accumulation, and the cyan region denotes electron depletion.

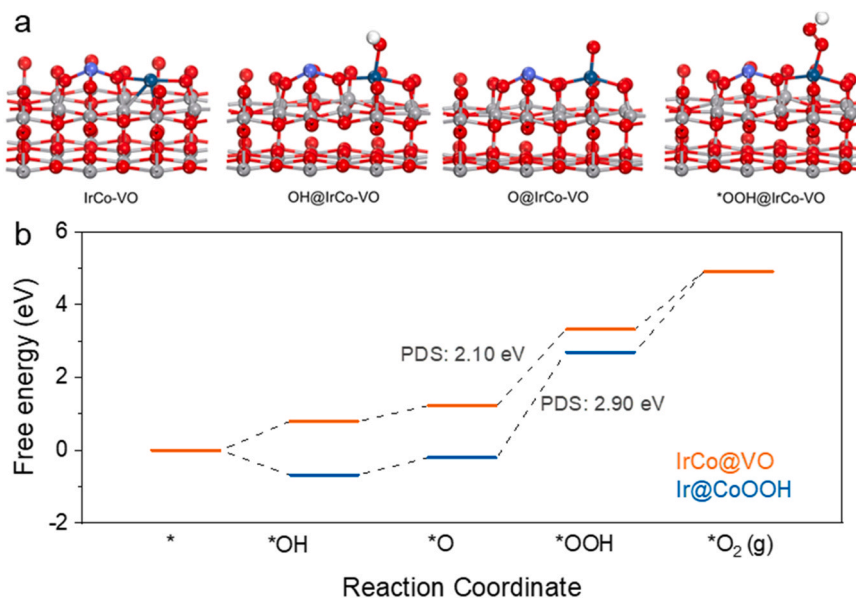


Fig. 6. (a) optimized structures of IrCo@VO with adsorption of different oxygen-containing intermediates, (b) Gibbs free energy diagrams of IrCo@VO and the referred Ir@CoOOH.

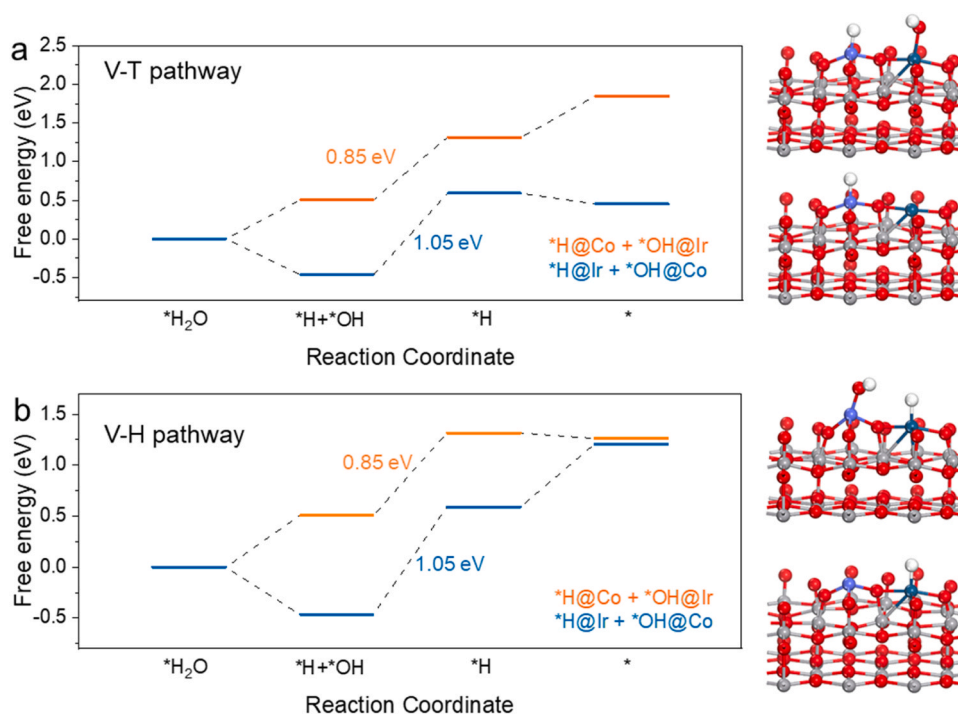


Fig. 7. (a) Volmer-Tafel pathway, (b) Vomer-Heyrovsky pathway of HER on IrCo@VO.

4. Conclusion

In this work, Ir-Co active species were confined in a two-dimensional tunnel structure provided by the layered V₂O₅. Thanks to the two-dimensional space accommodation, Ir-Co residing in between layers was expected to achieve good dispersion and low loading amount. This layered framework was further collapsed and disrupted in alkaline electrochemical conditions because of the inborn acidic nature of layered V₂O₅. The HER/OER active species of Co and Ir were quickly released and well exposed to the electrolyte, behaving like the ‘Trojan Horse’. The structure evolution of IrCo@VO in alkaline water splitting was monitored and elaborately examined by the *operando* Raman, XPS,

XRD and electrochemical characterizations. DFT calculations disclosed that the Ir was assigned as an OER active site instead of Co. The stabilization of Co was achieved merely by a Co–O covalent bond that caused a depletion of electrons around Co. Such an electrophilic center is more likely for the OH attack whereas not favorable for subsequent *OOH formation. Different from the case of Co, the neighbored Ir site was conjointly stabilized by a weak covalent bond with oxygen and a strong metal bond with V in the sublayer. The most intensified electron density overlap occurred between the Ir–V space. This leads to a less electron-deficient Ir that optimizes the binding energy with oxygen-containing intermediates *OH, *O and *OOH during the OER. In addition, for the HER catalysis in alkaline medium, the IrCo@VO shows a synergistic H₂O

dissociation by Co and Ir sites. The PDS was determined as an OH desorption step, despite a Volmer-Tafel or Volmer-Heyrovsky pathway that the H₂ evolution followed. The *in situ* exposed and transformed Co-Ir active species delivered an overpotential of 280 mV for OER and 90 mV for HER to achieve 10 mA cm⁻² current density. The IrCo@VO acted as both anode and cathode for better overall water splitting performance and stability compared to the commercial PtC/IrO₂ pair.

CRedit authorship contribution statement

YY. Pu conceived the idea, performed the experiments and calculations, wrote the manuscript. Y.F. Liu contributed to the data analysis and discussion. X.S. Tang contributed to the discussion of the results. Q. Huang provided experiment and data analysis support. L.M. Huang supervised the project and reviewed the paper. All authors contributed to the manuscript preparation.

Declaration of Competing Interest

The authors declare that they have no known competing financial interests or personal relationships that could have appeared to influence the work reported in this paper.

Data availability

Data will be made available on request.

Acknowledgements

This work was financially supported by Shenzhen Science and Technology Innovation Commission (JCYJ20220818100212027), Guangdong Provincial Key Laboratory of Catalysis (2020B121201002), Shenzhen Clean Energy Research Institute (CERI-KY-2019-003). The National Natural Science Foundation of China (Grant No. 22072010), Institute for Advanced Sciences (Grant No. E011A2022325). TEM, Raman data were obtained using equipment maintained by Southern University of Science and Technology Core Research Facilities. Natural Science Foundation of Chongqing for Distinguished Young Scholars (cstc2021jcyj-jqX0014), Chongqing Innovative Research Groups (No. CXQT20001). The National Natural Science Foundation of China (61975023, 62375032) CAS Interdisciplinary Innovation Team, and the Open Fund of the State Key Laboratory of High Field Laser Physics (Shanghai Institute of Optics and Fine Mechanic).

Appendix A. Supporting information

Supplementary data associated with this article can be found in the online version at [doi:10.1016/j.apcatb.2023.123319](https://doi.org/10.1016/j.apcatb.2023.123319).

References

- [1] Z.W. Seh, J. Kibsgaard, C.F. Dickens, I. Chorkendorff, J.K. Nørskov, T.F. Jaramillo, Combining theory and experiment in electrocatalysis: insights into materials design, *Science* 355 (2017).
- [2] L. Zhang, K. Doyle-Davis, X. Sun, Pt-Based electrocatalysts with high atom utilization efficiency: from nanostructures to single atoms, *Energy Environ. Sci.* 12 (2019) 492–517.
- [3] C.C.L. McCrory, S. Jung, J.C. Peters, T.F. Jaramillo, Benchmarking heterogeneous electrocatalysts for the oxygen evolution reaction, *J. Am. Chem. Soc.* 135 (2013) 16977–16987.
- [4] Y. Pu, L. Jia, Q. Huang, X. Tang, P. Rodriguez, L. Huang, Investigation on the surface charge separation in Pt-supported morphology-related-TiO₂ and its effect on water splitting, *J. Colloid Interface Sci.* 646 (2023) 815–823.
- [5] Y. Zhu, Q. Lin, Y. Zhong, H.A. Tahini, Z. Shao, H. Wang, Metal oxide-based materials as an emerging family of hydrogen evolution electrocatalysts, *Energy Environ. Sci.* 13 (2020) 3361–3392.
- [6] J. Song, C. Wei, Z.-F. Huang, C. Liu, L. Zeng, X. Wang, Z.-J. Xu, A review on fundamentals for designing oxygen evolution electrocatalysts, *Chem. Soc. Rev.* 49 (2020) 2196–2214.
- [7] S. Anantharaj, S. Kundu, S. Noda, “The Fe Effect”: a review unveiling the critical roles of Fe in enhancing OER activity of Ni and Co based catalysts, *Nano Energy* 80 (2021), 105514.
- [8] F. Dionigi, Z. Zeng, I. Sinev, T. Merzdorf, S. Deshpande, M.B. Lopez, S. Kunze, I. Zegkinoglou, H. Sarodnik, D. Fan, A. Bergmann, J. Drnec, J.Fd Araujo, M. Gliuch, D. Teschner, J. Zhu, W.-X. Li, J. Greeley, B.R. Cuenya, P. Strasser, In-situ structure and catalytic mechanism of NiFe and CoFe layered double hydroxides during oxygen evolution, *Nat. Commun.* 11 (2020) 2522.
- [9] D. Zhou, S. Wang, Y. Jia, X. Xiong, H. Yang, S. Liu, J. Tang, J. Zhang, D. Liu, L. Zheng, Y. Kuang, X. Sun, B. Liu, NiFe hydroxide lattice tensile strain: enhancement of adsorption of oxygenated intermediates for efficient water oxidation catalysis, *Angew. Chem. Int. Ed.* 58 (2019) 736–740.
- [10] Y. Pu, L. Wang, L. Jia, X. Li, W. Lu, L. Huang, Identifying the in situ protection role of MnO₂ nanosheets on Co oxide for superior water oxidation, *Appl. Surf. Sci.* 636 (2023), 157647.
- [11] J. Jiang, W. Ding, W. Li, Z. Wei, Freestanding single-atom-layer Pd-based catalysts: oriented splitting of energy bands for unique stability and activity, *Chem* 6 (2020) 431–447.
- [12] Y. Pu, M.J. Lawrence, V. Celorrio, Q. Wang, M. Gu, Z. Sun, L.A. Jácome, A. E. Russell, L. Huang, P. Rodriguez, Nickel confined in 2D earth-abundant oxide layers for highly efficient and durable oxygen evolution catalysts, *J. Mater. Chem. A* 8 (2020) 13340–13350.
- [13] J. Sanchez, M.B. Stevens, A.R. Young, A. Gallo, M. Zhao, Y. Liu, M.V. Ramos-Garcés, M. Ben-Naim, J.L. Colón, R. Sinclair, L.A. King, M. Bajdich, T.F. Jaramillo, Isolating the electrocatalytic activity of a confined NiFe motif within zirconium phosphate, *Adv. Energy Mater.* 11 (2021), 2003545.
- [14] J.P. Perdew, K. Burke, Y. Wang, Generalized gradient approximation for the exchange-correlation hole of a many-electron system, *Phys. Rev. B* 54 (1996) 16533–16539.
- [15] K. Kwapien, S. Piccinin, S. Fabris, Energetics of water oxidation catalyzed by cobalt oxide nanoparticles: assessing the accuracy of DFT and DFT+U approaches against coupled cluster methods, *J. Phys. Chem. Lett.* 4 (2013) 4223–4230.
- [16] B. Stahl, T. Bredow, Critical assessment of the DFT + U approach for the prediction of vanadium dioxide properties, *J. Comput. Chem.* 41 (2020) 258–265.
- [17] J. Wang, G. Li, D. Luo, Y. Zhao, Y. Zhang, G. Zhou, L. Shui, X. Wang, Amorphous–crystalline-heterostructured niobium oxide as two-in-one host matrix for high-performance lithium–sulfur batteries, *J. Mater. Chem. A* 9 (2021) 11160–11167.
- [18] C. Liu, Z. Neale, J. Zheng, X. Jia, J. Huang, M. Yan, M. Tian, M. Wang, J. Yang, G. Cao, Expanded hydrated vanadate for high-performance aqueous zinc-ion batteries, *Energy Environ. Sci.* 12 (2019) 2273–2285.
- [19] T. Gao, H. Fjellvåg, P. Norby, Raman scattering properties of a protonic titanate HxTi2-x/4□x/4O4-H2O (□, vacancy; x = 0.7) with lepidocrocite-type layered structure, *J. Phys. Chem. B* 112 (2008) 9400–9405.
- [20] C. Pasquini, L. D’Amario, I. Zaharieva, H. Dau, Operando Raman spectroscopy tracks oxidation-state changes in an amorphous Co oxide material for electrocatalysis of the oxygen evolution reaction, *J. Chem. Phys.* 152 (2020), 194202.
- [21] D. Chandra, D. Takama, T. Masaki, T. Sato, N. Abe, T. Togashi, M. Kurihara, K. Saito, T. Yui, M. Yagi, Highly efficient electrocatalysis and mechanistic investigation of intermediate IrOx(OH)y nanoparticle films for water oxidation, *ACS Catal.* 6 (2016) 3946–3954.
- [22] P.W. Menezes, A. Indra, A. Bergmann, P. Chernev, C. Walter, H. Dau, P. Strasser, M. Driess, Uncovering the prominent role of metal ions in octahedral versus tetrahedral sites of cobalt–zinc oxide catalysts for efficient oxidation of water, *J. Mater. Chem. A* 4 (2016) 10014–10022.
- [23] Y. Pu, V. Celorrio, J.M. Stockmann, O. Sobol, Z. Sun, W. Wang, M.J. Lawrence, J. Radnik, A.E. Russell, V.-D. Hodoroba, L. Huang, P. Rodriguez, Surface galvanic formation of Co-OH on Birnessite and its catalytic activity for the oxygen evolution reaction, *J. Catal.* 396 (2021) 304–314.
- [24] W. Chen, B. Wu, Y. Wang, W. Zhou, Y. Li, T. Liu, C. Xie, L. Xu, S. Du, M. Song, D. Wang, Y. Liu, Y. Li, J. Liu, Y. Zou, R. Chen, C. Chen, J. Zheng, Y. Li, J. Chen, S. Wang, Deciphering the alternating synergy between interlayer Pt single-atom and NiFe layered double hydroxide for overall water splitting, *Energy Environ. Sci.* 14 (2021) 6428–6440.
- [25] V. Pfeifer, T.E. Jones, J.J. Velasco Vélez, C. Massué, M.T. Greiner, R. Arrigo, D. Teschner, F. Girgsdies, M. Scherzer, J. Allan, M. Hashagen, G. Weinberg, S. Piccinin, M. Hävecker, A. Knop-Gericke, R. Schlögl, The electronic structure of iridium oxide electrodes active in water splitting, *Phys. Chem. Chem. Phys.* 18 (2016) 2292–2296.
- [26] I.T. McCrum, M.T.M. Koper, The role of adsorbed hydroxide in hydrogen evolution reaction kinetics on modified platinum, *Nat. Energy* 5 (2020) 891–899.